

Coordinated FCS-MPC and Auxiliary Damping Control for Enhanced SSR Mitigation in Series-Compensated DFIG Wind Farms

Le Van Dai*, Huynh Hoang Bao Nghia

Electric Power System Research Group, Faculty of Electrical Engineering Technology,
Industrial University of Ho Chi Minh City, Ho Chi Minh City, Vietnam

Received 03 November 2025; received in revised form 22 January 2026; accepted 23 January 2026

Abstract

This study proposes a comprehensive and novel coordinated control framework to effectively mitigate sub-synchronous resonance (SSR) in a doubly-fed induction generator based on wind turbines connected to series-compensated transmission lines. The proposed approach integrates finite control model predictive control in the rotor-side converter to achieve fast and accurate current tracking, while an SSR damping controller is embedded in the grid-side converter (GSC). Through coordinated operation, the GSC injects an auxiliary damping signal into the q -axis current reference to suppress sub-synchronous oscillations while maintaining DC-link voltage stability. Time-domain simulations conducted under diverse operating conditions demonstrate the robustness and superior performance of the proposed scheme. In particular, the total harmonic distortion is reduced from over 2.3% to below 2.0%, and the maximum electromagnetic torque oscillation is significantly suppressed from over 1.0 pu to approximately 0.02 pu, thereby confirming the effectiveness of the proposed control strategy in enhancing overall system stability.

Keywords: sub-synchronous resonance, doubly-fed induction generator, finite control set model predictive control, coordinated control, series-compensated transmission line

1. Introduction

The rapid pace of industrialization, coupled with the continuous growth in electricity demand, poses significant challenges to modern power grids. Conventional power generation systems, which remain heavily dependent on fossil fuels, are increasingly inadequate to satisfy these escalating energy requirements [1-2], while simultaneously exacerbating environmental concerns, particularly through greenhouse gas emissions [3-4]. As a result, the large-scale integration of renewable energy sources, especially wind power, has become a key pillar of global sustainable energy strategies [5-6]. Driven by advances in wind turbine technology and power electronics, large-scale wind farms are increasingly deployed and interconnected with national power systems through high-capacity alternating current transmission lines, enabling efficient long-distance power transmission and large-scale renewable energy penetration.

To optimize power transfer capacity and enhance long-distance transmission performance, series compensation capacitors are widely employed in high-voltage transmission lines. Despite their benefits, this practice introduces a critical technical challenge, commonly referred to as sub-synchronous resonance (SSR). SSR arises when the natural electrical resonance frequency of the series-compensated network interacts with the mechanical torsional modes of synchronous or asynchronous generators, resulting in sustained or growing electromechanical oscillations that threaten grid security and system stability [3-7].

* Corresponding author. E-mail address: levandai@iuh.edu.vn

SSR is widely recognized as one of the most critical forms of sub-synchronous interaction [8], particularly in power systems employing doubly-fed induction generator-based wind turbines (DFIG-WTs) [5-9]. Although DFIG-WTs exhibit relatively lower susceptibility to classical torsional interaction (TI) or torque amplification (TA) phenomena, the mitigation of SSR is still essential to ensure secure and reliable system operation, especially under series-compensated transmission conditions. The widespread occurrence and potential severity of SSR are further evidenced by numerous documented incidents reported worldwide, including several cases in Vietnam [10].

The mitigation of SSR in DFIG-based wind farms has become a prolific and active research topic in recent years. Existing SSR mitigation strategies are generally classified into three main categories: (i) the incorporation of supplementary damping controllers (SDCs) into DFIG converter control loops [11-12]; (ii) the optimization and fine-tuning SDC parameters using advanced optimization algorithms to enhance damping performance and robustness [13]; and (iii) the replacement of conventional proportional-integral (PI) controllers with advanced nonlinear or intelligent control techniques, such as predictive, adaptive, or robust control schemes [14].

While these approaches are capable of providing effective damping, most existing studies have primarily focused on optimizing the placement of the SDC either in the rotor-side converter (RSC) or the grid-side converter (GSC), as well as on selecting appropriate control signals to maximize SSR damping and improve power quality. Alternative mitigation strategies have also been explored, including the application of flexible AC transmission system devices [9] and the replacement of conventional phase-locked loops with advanced synchronization schemes, such as the double second-order generalized integrator phase-locked loop, to suppress SSR phenomena [15].

Owing to their low implementation cost and high flexibility, extensive research efforts have investigated the integration of SDCs into either the GSC or RSC of DFIG-WTs [11, 16-17]. Comparative analyses of optimal SDC placement indicate that GSC-based damping controllers employing capacitor voltage feedback generally achieve superior SSR mitigation performance. Furthermore, advanced control techniques, including adaptive control strategies and particle swarm optimization-based parameter tuning, have been employed to further enhance damping effectiveness and robustness [18]. In recent studies, control objectives have increasingly emphasized the simultaneous suppression of current harmonics and stabilization of the DC-link voltage, reflecting the growing demand for high power quality and robust dynamic performance in modern wind energy systems [19].

Model predictive control (MPC) has emerged as a significant advancement in the control of DFIG-WTs. Unlike conventional PI or field-oriented control schemes, MPC explicitly exploits the mathematical model of the DFIG to predict future system behavior, enabling the real-time selection of the optimal voltage vector based on a predefined cost function. This predictive and direct control capability significantly enhances dynamic performance, effectively reducing torque and current oscillations and lowering total harmonic distortion (THD), even under varying grid conditions and operating points.

Prior studies on SSR mitigation have predominantly relied on SDCs implemented in the RSC or on external power electronic devices. Such conventional approaches often require additional hardware, involve complex parameter tuning procedures, and, more importantly, fail to explicitly capture the coupled dynamic interactions between the RSC and GSC. As a result, a significant research gap exists regarding the coordinated integration of the rapid, optimizing capabilities of finite control set model predictive control (FCS-MPC) applied to the RSC together with an active SSR damping controller embedded in the GSC, particularly under challenging operating conditions such as variable wind speeds and high levels of series compensation. To address this gap, this paper proposes a novel coordinated control framework that synergistically integrates FCS-MPC-based RSC control with GSC-based SSR damping, aiming to achieve simultaneous SSR suppression, enhanced dynamic performance, and improved power quality.

This study develops a novel coordinated control framework that synergistically combines RSC-based FCS-MPC with GSC-integrated SSR damping (SSRD) for DFIG-WT systems connected to series-compensated transmission lines. The FCS-MPC enables the RSC to select the optimal voltage vector by minimizing a predefined cost function, thereby ensuring fast dynamic response and accurate current tracking, whereas the SSRD injects an auxiliary damping signal into the GSC q -axis current reference to effectively suppress sub-synchronous oscillations. To rigorously validate the proposed framework, theoretical modeling, modal analysis, and comprehensive time-domain simulations are performed using the MATLAB/Simulink environment, demonstrating robust and stable performance under a wide range of operating conditions, including variable wind speeds and high levels of series compensation.

The proposed control architecture clearly distinguishes itself from conventional PI-based coordinated strategies and existing MPC-based approaches by adopting a multi-layered damping mechanism. While traditional methods often suffer from strong control coupling between the RSC and GSC, the proposed framework exploits the fast dynamic response of FCS-MPC in the RSC to rapidly stabilize the internal machine variables, whereas the GSC-integrated SSRD is dedicated to suppressing the sub-synchronous components originating from the grid side. In contrast to recent MPC-based studies, which primarily focus on torque ripple reduction or current quality enhancement, the proposed coordinated RSC-GSC control scheme explicitly targets the mitigation of SSR by accounting for resonance frequency shifts, thereby providing a wider stability margin under high series-compensation levels.

The remainder of this paper is organized as follows. Section 2 describes the dynamic modeling of the DFIG-WT connected to a series-compensated transmission line and outlines the overall control architecture. Section 3 details the design of the FCS-MPC strategy for the RSC, emphasizing fast current tracking, along with the SSRD controller integrated into the GSC. Section 4 presents a simulation setup and evaluates the system performance under diverse operating conditions, including a comparative analysis of electromagnetic torque oscillation, active power dynamics, DC-link voltage stability, and harmonic distortion. Finally, Section 5 concludes the paper by summarizing the main findings, highlighting the key advantages of the proposed control framework, and discussing potential future research directions, such as hardware-in-the-loop validation and experimental implementation.

2. DFIG-based Wind Turbine Modeling

The power system under investigation, illustrated in Fig. 1, is adapted from the IEEE first benchmark model standard for SSR studies [20]. This system consists of a 100 MW DFIG-TW operating at 575 V, comprised of 50 WTs, each rated at 2 MW, and connected to the infinite bus through a 161 kV series-compensated transmission line and a 100 MVA, 575V/161kV step-up transformer [21]. The detailed electrical and mechanical parameters of the test system are summarized in Table 1.

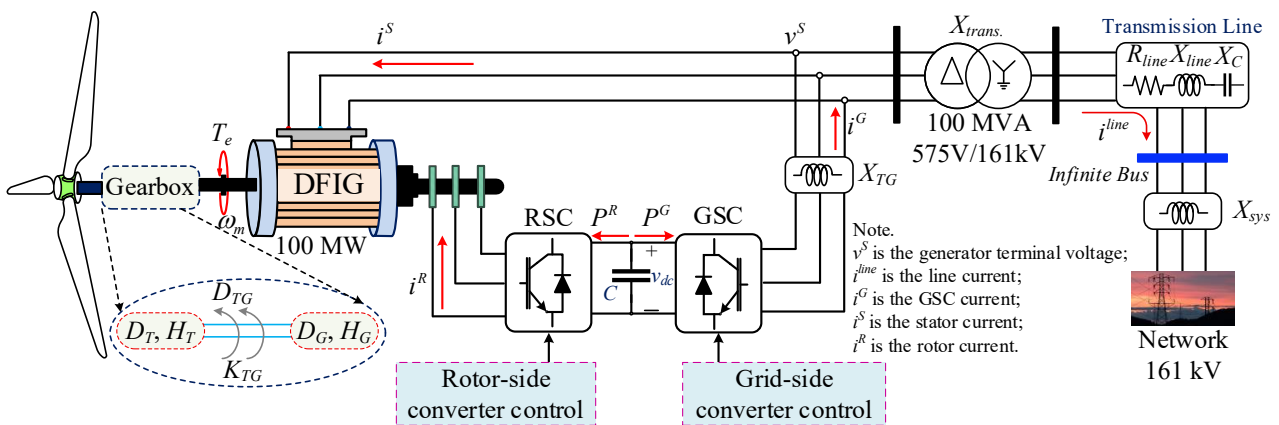


Fig. 1 Studied DFIG-WT system with series-compensated transmission line based on the IEEE SSR benchmark model

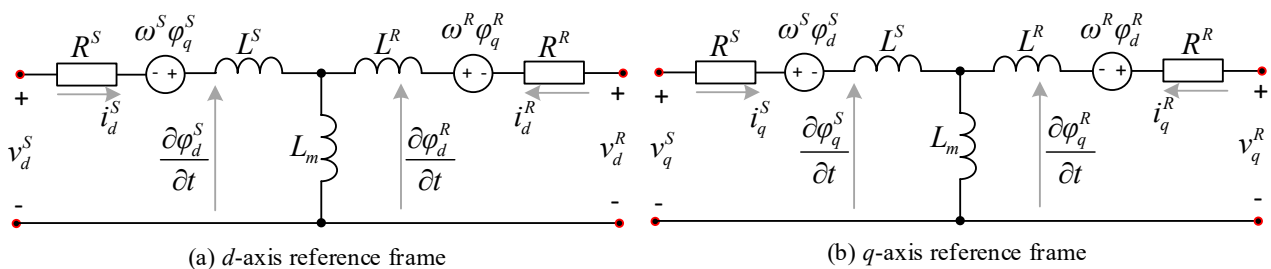
Table 1 Parameters of the studied DFIG-WT system

No.	Variable	Symbol	Value	Unit
I	161 kV transmission line and network			
1	The transmission line resistance	R_{line}	0.02	pu
2	The transmission line reactance	X_{line}	0.14	pu
3	The fixed series capacitor	X_C	64.8	Ohm
4	The system impedance	X_{sys}	0.06	pu
II	100 MVA 575V/161kV transformer			
1	The transformer reactance	$X_{trans.}$	0.14	pu
2	The transformer reactance in the GSC	X_{TG}	0.3	pu
III	Gear-box			
1	The damping coefficient of the turbine	D_T	0	pu
2	The inertia constants of the turbine	H_T	4.29	sec
3	The damping coefficient of the turbine-generator	D_{TG}	1.5	pu
4	The inertia constants of the turbine and generator	K_{TG}	0.15	pu
5	The damping coefficient of the generator	D_G	0	pu
6	The inertia constants of the generator	H_G	0.9	sec
IV	DFIG			
1	Rated power	P_r	100	MW
2	Rated voltage	V_r	575	V
3	Rated frequency	f_r	50	Hz
4	The stator resistances	R^S	0.023	pu
5	The rotor resistances	R^R	0.016	pu
6	The mutual inductance between the stator and rotor windings	L_m	2.9	pu
7	DC-link voltage	V_{dc}	1200	V
8	DC-link capacitor	-	10000	μF

2.1. Induction Generator

Fig. 2 illustrates the dq -axis equivalent circuit for the DFIG. To accurately describe the dynamic behavior of the DFIG, forward and inverse coordinate transformations are employed. By means of space vector analysis, the three-phase stator and rotor windings are transformed into equivalent two-phase representations in the synchronous rotating reference frame, which significantly simplifies the mathematical modeling and control design. Based on this framework, the stator voltage vectors are first defined, while the rotor voltage vectors are expressed in the dq reference frame and summarized as [4]

$$\begin{bmatrix} v_d^S \\ v_q^S \\ v_d^R \\ v_q^R \end{bmatrix} = \begin{bmatrix} R^S & 0 & 0 & 0 \\ 0 & R^S & 0 & 0 \\ 0 & 0 & R^R & 0 \\ 0 & 0 & 0 & R^R \end{bmatrix} \begin{bmatrix} i_d^S \\ i_q^S \\ i_d^R \\ i_q^R \end{bmatrix} + \frac{\partial}{\partial t} \begin{bmatrix} \varphi_d^S \\ \varphi_q^S \\ \varphi_d^R \\ \varphi_q^R \end{bmatrix} + \begin{bmatrix} -j\omega^S \varphi_q^S \\ j\omega^S \varphi_d^S \\ -j(\omega^S - \omega^R) \varphi_q^R \\ -j(\omega^S - \omega^R) \varphi_d^R \end{bmatrix} \quad (1)$$

Fig. 2 DFIG model in the dq reference frame

The flux linkages in the synchronous dq reference frame are expressed as [4, 6]

$$\begin{bmatrix} \varphi_d^S \\ \varphi_q^S \\ \varphi_d^R \\ \varphi_q^R \end{bmatrix} = \begin{bmatrix} L^S & 0 & L_m & 0 \\ 0 & L^S & 0 & L_m \\ L_m & 0 & L^R & 0 \\ 0 & L_m & 0 & L^R \end{bmatrix} \begin{bmatrix} i_d^S \\ i_q^S \\ i_d^R \\ i_q^R \end{bmatrix} \quad (2)$$

where $j = \begin{bmatrix} 0 & -1 \\ 1 & 0 \end{bmatrix}$; v_d^S and v_q^S denote the stator voltages in the dq -axis; v_d^R and v_q^R denote the rotor voltages in the dq -axis; i_d^S and i_q^S are the stator current in the dq -axis; i_d^R and i_q^R are the rotor current in the dq -axis; φ_d^S and φ_q^S represent the stator flux linkages in the dq -axis; φ_d^R and φ_q^R represent the rotor flux linkages in the dq -axis; R^S and R^R are the stator and rotor resistances; ω^S is the synchronous angular velocity of the rotating reference frame; ω^R is the angular velocity of the rotor; L^S and L^R are the stator and rotor self-inductances; p is the number of pole pairs; L_m is the mutual inductance between stator and rotor windings.

The electromagnetic torque of the DFIG is generated by the interaction between the stator and rotor magnetic fields in the synchronous dq reference frame. This interaction can be explicitly described using the dq -axis flux linkages and current components, which capture the electromechanical coupling of the system. Accordingly, the electromagnetic torque can be computed as [22]

$$T_e = \frac{3}{2} p \frac{L_m}{L^S} (\varphi_q^S i_d^R - \varphi_d^S i_q^R) \quad (3)$$

2.2. Wind Turbine Aerodynamics

The aerodynamic torque extracted from the wind, denoted as T_w , is determined by the incoming wind speed v_w . The relationship is calculated as [23-24]

$$T_w = \frac{0.5\pi\Re^2 \rho C_p v_w^2}{\omega_w} \quad (4)$$

where v_w denotes the wind velocity; ρ is the density of air; \Re is the turbine rotor radius, and ω_w represents the angular speed of the wind turbine rotor. The efficiency of wind energy capture is characterized by the power coefficient C_p , which depends on both the tip-speed ratio and the blade pitch angle, and is mathematically formulated as [25]

$$C_p = 0.5 \left(\frac{\Re C_f}{\lambda_w} - 0.022\theta - 2 \right) e^{-0.225 \frac{\Re C_f}{\lambda_w}} \quad (5)$$

where C_f is the blade design parameter, and θ denotes the pitch angle of the turbine blade. The tip-speed ratio λ_w , defined as the ratio between the blade tip speed and the wind speed, is given as

$$\lambda_w = \frac{\omega_w \Re}{v_w} \quad (6)$$

2.3. DC-Link Voltage

The dynamic behavior of the DC-link capacitor, which electrically couples the GSC and RSC, can be approximated by a first-order dynamic model, expressed as [10]

$$P^R + P^G = -Cv_{dc} \frac{\partial v_{dc}}{\partial t} \quad (7)$$

where v_{dc} denotes the DC-link voltage; C is the capacitance of the DC-link capacitor; P^R and P^G represent the active powers exchanged by the RSC and GSC, respectively. These power terms depend on the dq -axis voltage and current components, and can be equated as

$$\begin{cases} P^R = 0.5(v_d^R i_d^R + v_q^R i_q^R) \\ P^G = 0.5(v_d^G i_d^G + v_q^G i_q^G) \end{cases} \quad (8)$$

2.4. Shaft System

The two-mass drivetrain model is widely adopted as a standard framework for analyzing electromechanical dynamics and stability in wind energy conversion systems. In this model, the first mass represents the low-speed shaft dynamics of the wind turbine, whereas the second mass characterizes the high-speed shaft dynamics associated with the DFIG rotor. This configuration effectively captures the TI between the turbine and generator, which is critical for SSR analysis. The drivetrain dynamics can be expressed in the state-space form as [9]

$$\frac{\partial}{\partial t} \begin{bmatrix} \omega_w \\ \omega^R \\ T_{TG} \end{bmatrix} = \begin{bmatrix} \frac{-D_T - D_{TG}}{2H_T} & \frac{D_{TG}}{2H_T} & \frac{-1}{2H_T} \\ \frac{D_{TG}}{2H_G} & \frac{-D_G - D_{TG}}{2H_G} & \frac{-1}{2H_G} \\ K_{TG}\omega_b & -K_{TG}\omega_b & 0 \end{bmatrix} \begin{bmatrix} \omega_w \\ \omega^R \\ T_{TG} \end{bmatrix} + \begin{bmatrix} \frac{1}{2H_T} & 0 & 0 \\ 0 & \frac{-1}{2H_G} & 0 \\ 0 & 0 & 1 \end{bmatrix} \begin{bmatrix} T_w \\ T_e \\ 0 \end{bmatrix} \quad (9)$$

This two-mass drivetrain model characterizes the dynamic interaction between the turbine and generator through shaft inertia, damping, and torsional stiffness parameters. The formulation explicitly captures the exchange between mechanical torque and electromagnetic torque, which is essential for analyzing low-frequency torsional oscillations and SSR phenomena. The parameters are summarized in Table 1.

2.5. Transmission Line Model

The dynamic behavior of the series-compensated transmission line is represented using a state-space model in which the transmission line currents and the voltage across the series capacitor are selected as the state variables. This formulation captures the essential electrical dynamics associated with series compensation and can be expressed as [21]

$$\frac{\partial}{\partial t} \begin{bmatrix} i_q^{line} \\ i_d^{line} \\ v_q^C \\ v_d^C \end{bmatrix} = \begin{bmatrix} -\frac{R_{line}}{X_{line}} & -\omega^S & -\frac{1}{X_{line}} & 0 \\ \omega^S & -\frac{R_{line}}{X_{line}} & 0 & -\frac{1}{X_{line}} \\ X_C & 0 & \omega^S & 0 \\ 0 & X_C & \omega^S & 0 \end{bmatrix} \begin{bmatrix} i_q^{line} \\ i_d^{line} \\ v_q^C \\ v_d^C \end{bmatrix} + \begin{bmatrix} \omega_b & 0 & 0 & 0 \\ 0 & \omega_b & 0 & 0 \\ 0 & 0 & 1 & 0 \\ 0 & 0 & 0 & 1 \end{bmatrix} \begin{bmatrix} \frac{v_q^S - E_q^B}{X_{line}} \\ \frac{v_d^S - E_d^B}{X_{line}} \\ 0 \\ 0 \end{bmatrix} \quad (10)$$

where i_d^{line} and i_q^{line} denote the transmission line dq -axis currents; v_d^C and v_q^C represent the series capacitor's dq -axis voltages; R_{line} and X_{line} are the resistance and reactance of the transmission line, respectively; X_C denotes the fixed-series capacitor; E_d^B and E_q^B are the dq -axis voltages of the infinite bus. The synchronous angular frequency is denoted by ω^S .

2.6. Rotor- and Grid- Side Converters

The RSC and GSC constitute the core power electronic interface of the DFIG system, enabling decoupled control of machine-side electromagnetic variables and grid-side power exchange. The RSC primarily regulates the rotor currents to control the electromagnetic torque and stator reactive power, whereas the GSC is responsible for maintaining the DC-link voltage and managing reactive power exchange with the grid. Accurate modeling and coordinated control of these two converters are therefore essential for stable operation and effective mitigation of SSR in series-compensated DFIG-WT systems.

This study develops control-oriented models for both the RSC and GSC. To achieve optimal performance in DFIG-WTs, maximum power point tracking (MPPT) techniques are employed, as reported in [26-27]. Fig. 3 illustrates the relationship between wind power output and turbine rotor speed under different wind velocities, highlighting the MPPT operating trajectory. Under MPPT operation, the control system computes the optimal reference values of active power and rotor speed corresponding to a given wind speed. However, practical constraints imposed by converter capacity and turbine torque limits may prevent strict adherence to the MPPT trajectory. At low wind speeds, the DFIG typically operates at a nearly fixed rotor speed, whereas at higher wind speeds exceeding the turbine torque limit, the system transitions to a constant-torque operating model.

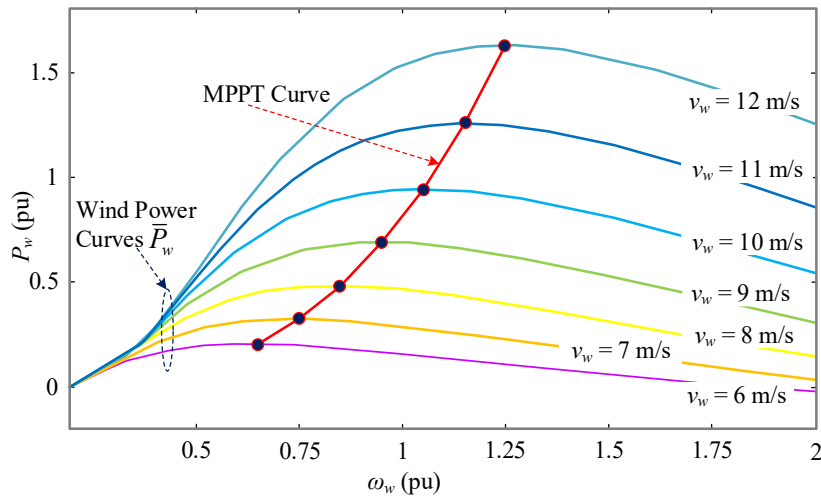


Fig. 3 Wind turbine power-speed characteristics and MPPT trajectory for varying wind speeds

In this framework, the primary roles of the RSC and GSC are to facilitate DFIG operation along the desired MPPT trajectory whenever feasible. Both converters are modeled without explicit energy storage elements, allowing converter losses to be neglected and enabling a focus on the dominant electromechanical dynamics. Furthermore, the high-frequency switching behavior of the power converters is approximated using an average-value model, which is appropriate for analyzing sub-synchronous phenomena in the frequency range of 5-40 Hz. Although this modeling approach neglects ultra-fast switching transients and switching losses, the high sampling frequency employed in the FCS-MPC strategy with 20 kHz ensures accurate discrete-time predictions. Consequently, the impact of the neglected high-frequency dynamics on the overall SSR damping performance is minimal, as confirmed by the close agreement between theoretical modal analysis and time-domain simulation results.

Figs. 4 and 5 present the schematic control structures of the RSC and GSC, respectively. The RSC regulates the electromagnetic torque T_e and the stator reactive power Q_s . Under steady-state conditions and neglecting losses, the mechanical torque extracted from the wind satisfies $T_w = P_w/\omega_w$, which balances the electromagnetic torque, T_e . Accordingly, the torque reference T_{e_ref} is derived from the MPPT-based mechanical torque reference T_{e_ref} , as illustrated in Fig. 4. The stator reactive power reference Q_{s_ref} is determined by the selected reactive power strategy, such as constant reactive power or unity power

factor operation, with this study adopting the unity power factor approach. Additionally, the GSC is responsible for regulating the DC-link voltage and the terminal voltage of the induction machine. Overall, the inclusion of the RSC and GSC control loops introduces eight additional state variables into the overall system model, corresponding to the internal states of the PI regulators, which are collectively represented in the system state vector [28].

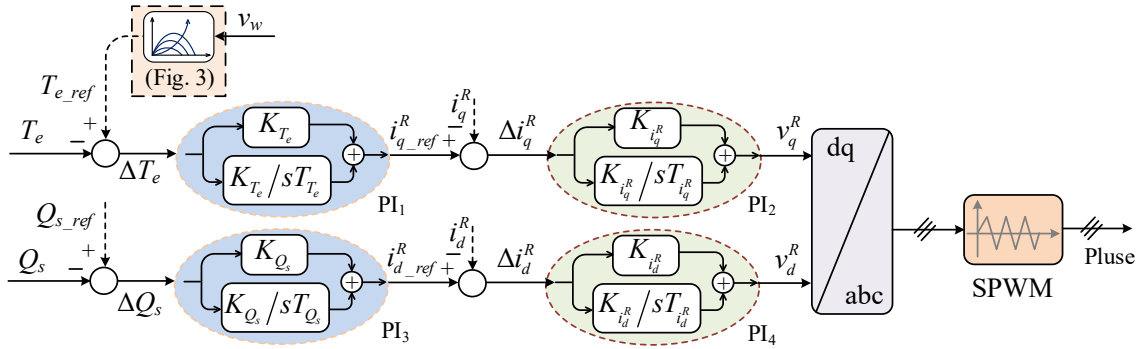


Fig. 4 The rotor-side converter controller

The RSC controller adopts a dual-loop control structure, as illustrated in Fig. 4. The inner control loop regulates the dq -axis components of the rotor current, whereas the outer control loop independently governs the active and reactive power of the DFIG. The dynamic behavior of the RSC controller is described by the corresponding control model, with the associated controller parameters summarized in Table 2. Similarly, the GSC employs a dual-loop control architecture, as depicted in Fig. 5. The inner loop controls the dq -axis components of the GSC, while the outer loop is responsible for regulating both the DC-link voltage and the stator terminal voltage. The control parameters of the GSC are provided in Table 3.

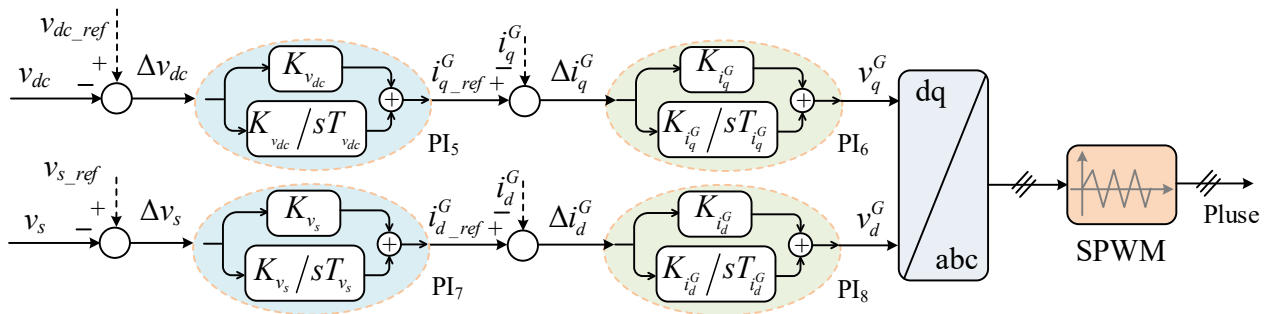


Fig. 5 The grid-side converter controller

Table 2 Parameters of the rotor-side converter control system

Torque control loop		q -axis current control loop		Reactive power control loop		d -axis current control loop	
K_{T_e}	T_{T_e}	$K_{i_q^R}$	$T_{i_q^R}$	K_{Q_s}	T_{Q_s}	$K_{i_d^R}$	$T_{i_d^R}$
0.0001	0.05	0.12	0.12	0.0001	0.025	0.12	1.2

Table 3 Parameters of the grid-side converter control system

DC voltage control loop		q -axis current control loop		Voltage control loop		d -axis current control loop	
$K_{v_{dc}}$	$T_{v_{dc}}$	$K_{i_q^G}$	$T_{i_q^G}$	K_{v_s}	T_{v_s}	$K_{i_d^G}$	$T_{i_d^G}$
8	400	0.83	5	1.55	5	0.83	5

2.7. The Sub-Synchronous Resonance Phenomenon

SSR occurs in power systems due to the exchange of energy between the mechanical components of the turbine-generator and the electrical network. This energy transfer takes place at one or more natural frequencies inherent to the coupled system.

SSR can result in significant problems within the power system. The phenomenon involves rotor currents that induce asynchronous voltage components in the armature, which in turn can amplify the asynchronous armature current, leading to SSR. The primary categories of SSR are induction generator effect (IGE), TI, and TA. The subsequent sections of this study provide a concise overview of these different SSR types.

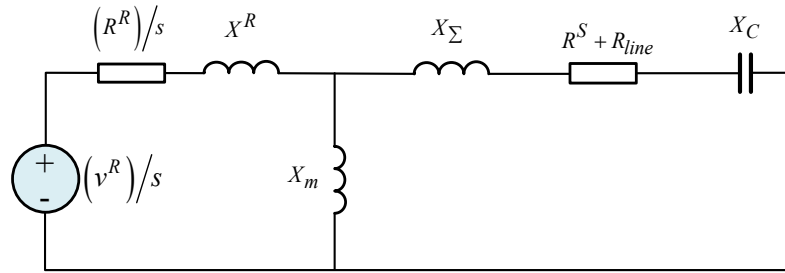


Fig. 6 Equivalent circuit of the DFIG connected to a series-compensated network for SSR analysis

TI refers to the dynamic interaction between the mechanical vibration of the turbine-generator shaft and the power system. TI is one of the primary SSR phenomena that must be carefully analyzed and mitigated in systems with series compensation or other configurations prone to SSR. TA refers to the sudden and temporary torque fluctuations that occur in the turbine-generator shaft during disturbances or changes in operating conditions. IGE occurs when the turbine-generator operates in a mode similar to an induction generator, usually under sub-synchronous conditions. In a series-compensated power system, the compensation level is characterized by the ratio $k = X_C / (X_{line} + X_{trans.})$. This configuration can induce sub-synchronous currents at a frequency determined by the expression provided in [10]

$$\begin{cases} f_{ne} = f_s \sqrt{\frac{X_C}{X_\Sigma}} \\ X_\Sigma = X^S + X_{line} + X_{trans.} + X_{sys.} \end{cases} \quad (11)$$

where f_{ne} is the natural frequency of the electrical system and f_s is the system's fundamental frequency. At this particular frequency, the slip value described $s = (\omega^S + \omega^R) / \omega^S$ becomes negative, resulting in a negative electrical resistance at the sub-synchronous frequency. This tends to amplify the sub-synchronous current over time, a behavior known as the IGE. The rotor current frequency, f_{re} can lead to negative electrical resistance in the stator, which is transferred to the rotor through the magnetic field [10]. This equation can be represented as

$$f_{re} = sf_s \quad (12)$$

Fig. 6 illustrates the steady-state equivalent circuit of the system operating at a sub-synchronous frequency. When the absolute value of the equivalent rotor resistance, expressed as $R^R/s < 0$ when the resistance of the armature and the network become greater than the combined resistance, a negative resistance appears at the sub-synchronous frequency. This condition causes the sub-synchronous current to grow over time, a behavior known as the IGE.

3. Proposed Control Method

This section presents the proposed control methodology for the DFIG-WT system, with emphasis on enhancing SSR damping and dynamic performance. The control framework integrates an SDC with an advanced predictive control strategy to improve robustness under varying operating conditions. The detailed modeling and control design of each converter are introduced sequentially to provide a clear understanding of the proposed approach.

3.1 Rotor-Side Converter

The RSC plays a key role in regulating the rotor currents and electromagnetic torque of the DFIG, thereby directly affecting the system dynamic performance. To facilitate the design of a predictive current controller, an explicit mathematical description of the rotor current dynamics is required. Starting from the voltage and flux linkage equations of the DFIG, the current dynamics are reformulated into a continuous-time state-space representation. Substituting Eq. (2) into Eq. (1) and arranging the current derivatives, the continuous-time state-space model of the DFIG current dynamics can be formulated as [14, 25, 29]

$$\frac{\partial}{\partial t} \begin{bmatrix} i_d^S \\ i_q^S \\ i_d^R \\ i_q^R \end{bmatrix} = \underbrace{\begin{bmatrix} -\frac{R^S}{L^S} & j\omega^S & \frac{R^S L_m}{L^S L^R} & j(\omega^S - \omega^R) \frac{L_m}{L^S} \\ -j\omega^S & -\frac{R^S}{L^S} & -j(\omega^S - \omega^R) \frac{L_m}{L^S} & \frac{R^S L_m}{L^S L^R} \\ \frac{R^R L_m}{L^S L^R} & 0 & -\frac{R^R}{L^R} & j(\omega^S - \omega^R) \\ 0 & \frac{R^R L_m}{L^S L^R} & -j\omega_{SR} & -\frac{R^R}{L^R} \end{bmatrix}}_{\mathbf{A}} \begin{bmatrix} i_d^S \\ i_q^S \\ i_d^R \\ i_q^R \end{bmatrix} + \underbrace{\begin{bmatrix} \frac{1}{L^S} & 0 & L_m & 0 \\ 0 & \frac{1}{L^S} & 0 & L_m \\ L_m & 0 & \frac{1}{L^R} & 0 \\ 0 & L_m & 0 & \frac{1}{L^R} \end{bmatrix}}_{\mathbf{B}} \begin{bmatrix} v_d^S \\ v_q^S \\ v_d^R \\ v_q^R \end{bmatrix} \quad (13)$$

The fundamental principle of the FCS-MPC technique is to predict the system's future behavior using a discrete-time mathematical model over a finite control horizon. Within each sampling period, the controller evaluates the dynamic evolution of key variables such as voltages, currents, fluxes, torque, and power based on all admissible switching states of the converter. This predictive mechanism allows the controller to determine the optimal switching state that minimizes the predefined cost function at the next sampling instant ($k + 1$). To construct the prediction model, the continuous-time representation of the DFIG system can be expressed as

$$\frac{\partial x(t)}{\partial t} = \mathbf{A}x(t) + \mathbf{B}u(t) \quad (14)$$

where $x(t)$ and $u(t)$ denote the state and control input vectors, respectively, while \mathbf{A} and \mathbf{B} represent the continuous-time system matrices incorporating electrical parameters such as stator/rotor inductances, resistances, and mutual coupling effects. By applying the Euler forward discretization method with a sampling period T_s , the discrete-time model is obtained as

$$x(k+1) = x(k) + T_s \left. \frac{\partial x(t)}{\partial t} \right|_{t=k} \quad (15)$$

Substituting Eq. (14) into Eq. (15) yields the discrete dynamic equation:

$$x(k+1) = (\mathbf{I} + \mathbf{A}T_s)x(k) + \mathbf{B}T_s u(k) \quad (16)$$

where \mathbf{I} is the identity matrix of the same dimension as \mathbf{A} . Given the finite number of switching states $S_i (i = 1, \dots, n)$, the predictive control problem is then formulated as an optimization task. At each sampling period, all possible switching vectors are simulated through Eq. 19, and the resulting predicted states are evaluated by a cost function that quantifies the deviation between predicted and reference quantities. The control action that minimizes this cost function is applied to the converter at the next interval ($k + 1$).

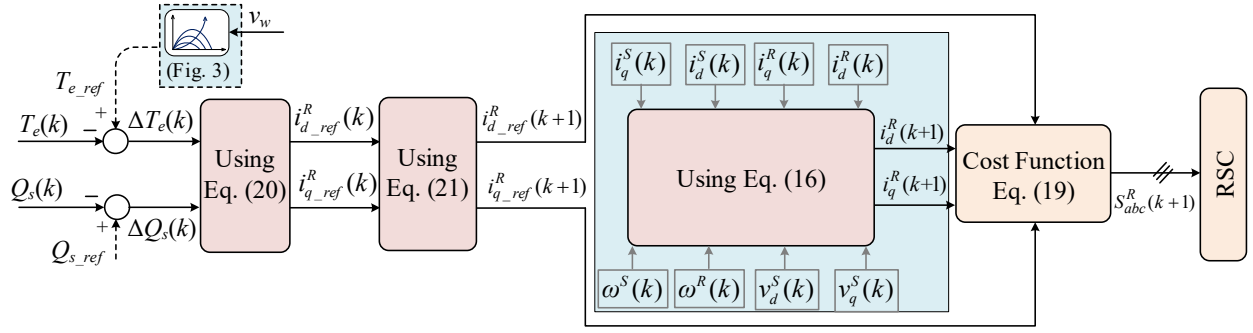


Fig. 7 The proposed control strategy of the rotor-side converter

The proposed cost function is designed to ensure both dynamic accuracy and computational efficiency, expressed generically as

$$\text{cost}(k) = \|x_{ref}(k+1) - x_p(k+1)\| \quad (17)$$

where $x_{ref}(k+1)$ represents the extrapolated reference trajectory and $x_p(k+1)$ denotes the predicted state at $(k+1)^{\text{th}}$ sampling instant. Depending on the control objective, the cost function evaluated at the prediction step $(k+1)$ can adopt absolute, quadratic, or exponential weighting forms, expressed respectively as

$$\begin{cases} \text{cost}(k) = |x_{ref}(k+1) - x_p(k+1)| \\ \text{cost}(k) = (x_{ref}(k+1) - x_p(k+1))^2 \\ \text{cost}(k) = e^{|x_{ref}(k+1) - x_p(k+1)|} \end{cases} \quad (18)$$

However, the exponential form often entails a higher computational load, making it less favorable for real-time execution. For current regulations in DFIG systems, a simplified quadratic cost function is typically employed. The RSC cost function can be presented as

$$\text{cost}_{RSC} = (i_{d_ref}^R(k+1) - i_d^R(k+1))^2 + (i_{q_ref}^R(k+1) - i_q^R(k+1))^2 \quad (19)$$

In this context, $i_{d_ref}^R$ and $i_{q_ref}^R$ represent the reference values for the rotor current components along the dq -axis, respectively. The reference rotor current along the q -axis is directly related to the electromagnetic torque control, since the torque of the DFIG is primarily influenced by the q -axis component of the rotor current. The equation can be expressed as

$$\begin{cases} i_{q_ref}^R(k) = \frac{2}{3} \frac{\omega^S(k)L^S}{pv_d^S(k)L_m} \underbrace{(T_{e_ref}(k) - T_e(k))}_{\Delta T_e(k)} \\ i_{d_ref}^R(k) = \frac{2}{3} \frac{L^S}{v_d^S(k)L_m} \underbrace{(Q_{e_ref}(k) - Q_e(k))}_{\Delta Q_e(k)} - \frac{v_d^S(k)}{\omega^S(k)L^S} \end{cases} \quad (20)$$

To enhance the prediction capability of the MPC scheme, an accurate estimation of the reference current trajectory at the next sampling instant is required. Since the reference signals vary continuously with operating conditions, direct usage of instantaneous references may degrade prediction accuracy. Therefore, the reference currents for the next sampling period are estimated to use Lagrange extrapolation as

$$\begin{cases} i_{q_ref}^R(k+1) = 2i_{q_ref}^R(k) - i_{q_ref}^R(k-1) \\ i_{d_ref}^R(k+1) = 2i_{d_ref}^R(k) - i_{d_ref}^R(k-1) \end{cases} \quad (21)$$

This approach ensures that the reference trajectory of the rotor current evolves smoothly across sampling periods, thus enhancing the overall predictive control performance. The MPC algorithm follows a structured computational process; the control structure is shown in Fig. 7.

3.2 Grid-Side Converter

The control structure of the GSC with integrated SSRD aims to maintain the DC-link voltage stability, regulate reactive power exchange, and simultaneously mitigate sub-synchronous oscillations through dynamic torque damping. The GSC control is implemented in the synchronous dq -reference frame oriented along the grid voltage vector. In this configuration, the q -axis component of the converter current controls the active power flow, thereby maintaining the DC-link voltage at its reference value, while the d -axis component regulates the reactive power or grid voltage at the point of common coupling (PCC). The dynamic equations of the GSC filter in the dq -reference frames are given by:

$$\begin{cases} v_d^G = R_f i_d^G + L_f \frac{\partial i_d^G}{\partial t} - \omega^S L_f i_q^G + v_d^{\text{grid}} \\ v_q^G = R_f i_q^G + L_f \frac{\partial i_q^G}{\partial t} - \omega^S L_f i_d^G + v_q^{\text{grid}} \end{cases} \quad (22)$$

where R_f and L_f are the filter parameters, v_d^{grid} and v_q^{grid} are the grid voltage components. The fundamental approach to reducing SSR involves producing electromagnetic torque that counteracts the rotor's speed, as expressed in Eq. (3). Therefore, a controller is required to reduce SSR by regulating these parameters. Two methods exist for damping SSR using such controllers: the first involves incorporating the additional controller into the RSC, while the second integrates it with the GSC. Therefore, this paper proposes a GSC control method by applying a damping controller to address this phenomenon. Fig. 8 shows the location of the SSRD in the GSC. The dynamic behavior of this damping controller is represented as [27]

$$\text{OCS}_{\text{sat}} = \underbrace{(\omega_{r_ref} - \omega_r)}_{\Delta\omega_r} \left(K_{SSRD} + \frac{K_{SSRD}}{sT_{SSRD}} \right) \quad (23)$$

where K_{SSRD} represents the proportional gain of the damping controller, and T_{SSRD} defines the dynamic phase compensation time constant. The signal OCS is saturated within the range $[-\text{OCS}_{\text{min}}, +\text{OCS}_{\text{max}}]$ to prevent overmodulation and instability. This signal is added to the reference of the q -axis current, yielding

$$\text{OCS}_{\text{sat}} = \begin{cases} +\text{OCS}_{\text{max}} & \left\{ \begin{array}{l} \text{OCS} > +\text{OCS}_{\text{max}} \\ \text{OCS} < -\text{OCS}_{\text{min}} \end{array} \right. \\ -\text{OCS}_{\text{min}} \\ \text{OCS} & \text{otherwise} \end{cases} \quad (24)$$

The output of the SSRD block is added directly to the q -axis current reference from the DC-link controller, forming the composite reference [27]

$$\Delta i_q^G = i_{q_ref}^G - i_q^G + \text{OCS}_{\text{sat}} \quad (25)$$

This reference is then compared with the measured i_q^G , and the error signal is processed by the current controller, which can be expressed as

$$\begin{cases} v_d^G = (K_{i_d^G} + \frac{K_{i_d^G}}{sT_{i_d^G}})(i_{d_ref}^G - i_d^G) - \omega^S L_f i_q^G \\ v_q^G = (K_{i_q^G} + \frac{K_{i_q^G}}{sT_{i_q^G}})(i_{q_ref}^G - i_q^G + OCS_{sat}) - \omega^S L_f i_d^G \end{cases} \quad (26)$$

The reference voltages v_d^G and v_q^G are then transformed back to the three-phase frame through inverse park and Clarke transformations and fed to the sinusoidal pulse width modulation (SPWM) generator to produce gating signals for the converter switches in Fig. 8.

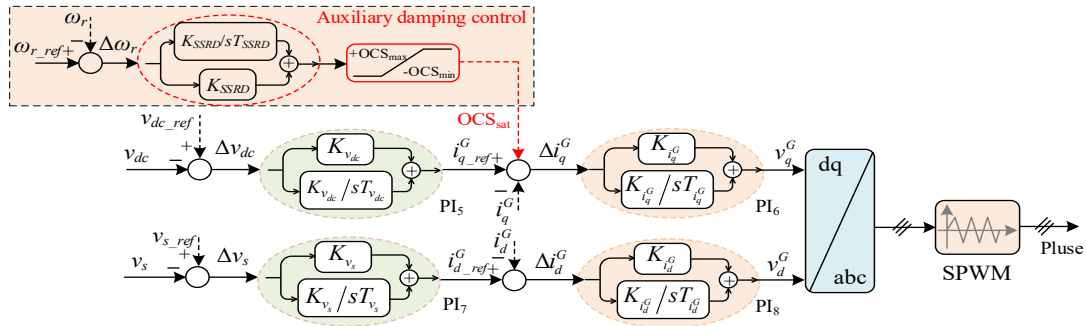


Fig. 8 The proposed control strategy of the grid-side converter

From the control perspective, the inclusion of OCS_{sat} modifies the q -axis current reference, enabling the converter to inject an active current component that counteracts the sub-synchronous component of the rotor speed oscillation. The instantaneous damping torque contribution can be computed as

$$\Delta T_{damp} = K_T OCS_{sat} \quad (27)$$

and in the frequency domain is represented as

$$\Delta T_{damp}(s) = K_T OCS_{sat} (1 + sT_{SSRD}) \Delta \omega_r(s) \quad (28)$$

To ensure effective damping, the real part of the damping transfer function is evaluated at the SSR frequency of ω_{fs} , which must satisfy the following stability conditions:

$$\text{Real}\{K_T K_{SSRD} (1 + jT_{SSRD} \omega_{fs})\} > 0 \quad (29)$$

where K_T denotes the torque constant. Under this condition, as shown in Eq. (29), the injected current component generates an electromagnetic torque that is consistently opposite in phase to the sub-synchronous oscillation, thereby dissipating oscillatory energy from the mechanical system and enhancing overall dynamic stability. This control configuration allows the GSC to perform its conventional functions of DC-link voltage regulation and reactive power control, while simultaneously providing effective active damping for SSR, without affecting steady-state operating conditions. The integration of SSRD within the existing control structure ensures fast dynamic response, decoupled power regulation, and robust suppression of sub-synchronous oscillations in series-compensated DFIG systems. These observations indicate that rotor angular velocity plays a crucial role in the development and mitigation of SSR phenomena. Consequently, the rotor angular velocity is selected as the input signal for the SSRD controller.

The tuning of SSRD parameters, namely K_{SSRD} and T_{SSRD} , is carried out through a frequency-scanning and phase-compensation procedure. First, the resonant frequency f_{ne} is identified using fast Fourier transform analysis of the rotor current. Subsequently, the time constant T_{SSRD} is calculated to ensure that the injected damping signal leads the speed deviation by an optimal phase angle, thereby emulating a virtual resistance in the sub-synchronous frequency range. The gain K_{SSRD} is then fine-tuned through sensitivity analysis to achieve maximum damping without violating the converter current limits. In this study, K_{SSRD} is set to 1.55, and T_{SSRD} is chosen as 5, in accordance with the guidelines reported in [26-27].

4. Verification Analysis

Since the actual dynamic response of the system under disturbance can be captured through time domain simulation, the proposed SSRD is implemented in the internal current control loops of GSC using MATLAB/Simulink in Fig. 9. To validate the ability to mitigate SSR, the proposed SSRD is tested under different compensation levels and different wind speed conditions. The control parameters are summarized in Tables 1-3. Therefore, this study evaluates three typical simulation cases as follows: (i) Case study 1: Wind speed of 7 m/s and compensation level up to 50%; (ii) Case study 2: Wind speed of 9 m/s and compensation level up to 50%; (iii) Case study 3: Wind speed of 11 m/s and compensation level up to 30%. The content will be presented in detail in the following subsections.

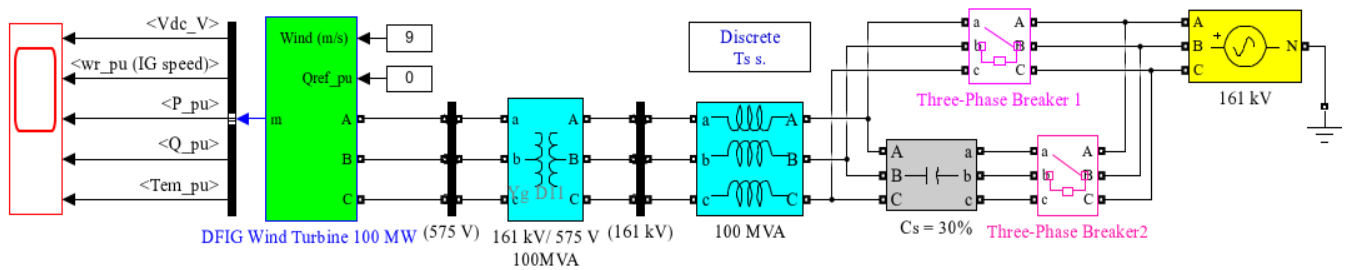
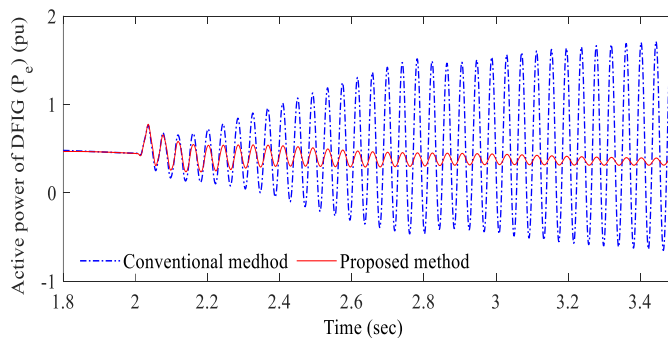


Fig. 9 MATLAB/Simulink test model for SSR mitigation in a DFIG-WT system

4.1. Case Study 1, Wind Speed of 7 m/s and Compensation Level up to 50%

Initially, the system operates at a low compensation level of 10%, where it remains stable. At time $t = 2$ sec, the compensation level is increased to 50%, as illustrated in Fig. 10, under a wind speed of 7 m/s. The dynamic responses of the active power P_e , electromagnetic torque T_e , and DC link voltage V_{dc} from the DFIG wind turbine are presented in Fig. 8, while the harmonic spectrum is shown in Fig. 11. When the compensation level is raised at $t = 2$ sec, SSR emerges in the system's dynamic response, as observed in Fig. 10. However, the proposed SSRD effectively suppresses SSR across all tested compensation levels, with the fluctuations in T_e , and V_{dc} gradually returning to their nominal values. Conversely, at a 70% compensation level, Fig. 10 demonstrates that the conventional method fails to mitigate SSR, whereas the proposed SSRD successfully dampens the oscillations.



(a) Active power

Fig. 10 Dynamic responses of the DFIG-WT system under Case Study 1

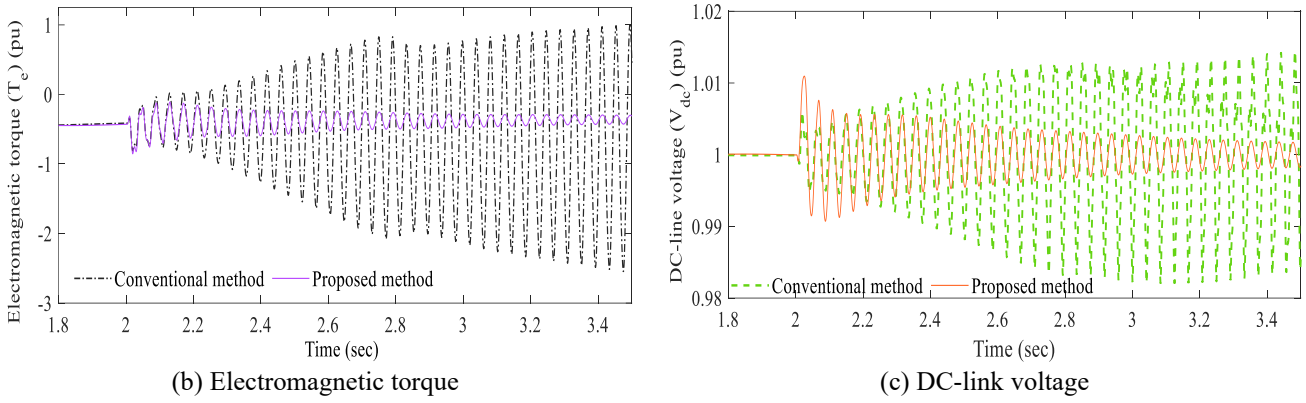


Fig. 10 Dynamic responses of the DFIG-WT system under Case Study 1 (continued)

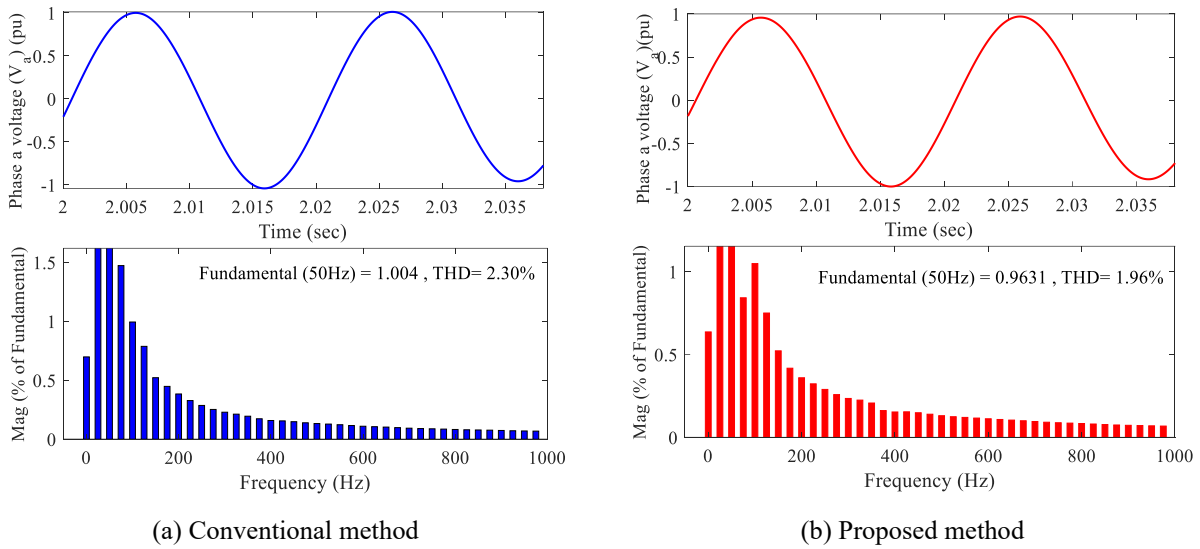


Fig. 11 Phase A voltage waveform and harmonic spectrum at the 575 V bus under Case Study 1

The simulation outcomes with and without the SSRD align well with the eigenvalue analysis summarized in Table 4. Notably, the SSRD exhibits superior damping performance by significantly reducing the oscillation decay time compared to the conventional SDC. Additionally, the active power P_e shows substantially reduced peak values under the proposed method, with a maximum of 0.9594 pu and a minimum of -0.7675 pu, whereas the conventional approach exhibits much larger extremes of 2.632 pu and -1.454 pu. Moreover, the harmonic distortion decreases from 2.30% using the conventional method to 1.96% with the proposed approach, indicating that the improved damping performance is accompanied by enhanced power quality and reduced oscillatory behavior.

Table 4 Statistical comparison of key signals during 2.0 to 3.5 sec under Case Study 1

Parameters	Signal statistics	Proposed method	Conventional method	Parameters	Signal statistics	Proposed method	Conventional method
P_e (pu)	max	9.594e-01	2.632e+00	V_{dc} (pu)	max	1.047e+00	1.364e+00
	min	-7.675e-01	-1.454e+00		min	9.168e-01	8.822e-01
T_e (pu)	max	1.890e-02	1.353e+00	%THD	-	1.96	2.30
	min	-9.937e-01	-5.418e+00	-	-	-	-

Similarly, the electromagnetic torque T_e experiences significantly smaller oscillations when the proposed controller is applied, with a maximum of 0.0189 pu and a minimum of -0.9937 pu, compared to the conventional method, which produces large swings between 1.353 pu and -5.418 pu. Regarding the DC-link voltage V_{dc} , the proposed method maintains values closer to the nominal level, with peaks of 1.047 pu and troughs of 0.9168 pu, while the conventional case exhibits wider deviations,

reaching 1.364 pu and dropping to 0.8822 pu. Furthermore, the harmonic distortion decreases from 2.30% using the conventional method to 1.96% with the proposed approach, confirming that the proposed strategy not only improves dynamic stability but also yields cleaner waveforms and better overall power quality.

4.2. Case Study 2, Wind Speed of 9 m/s and Compensation Level up to 50%

The effectiveness of the proposed SSRD was evaluated at a wind speed of 9 m/s, with a constant compensation level of 50% applied at $t = 2$ sec for all considered scenarios. The comparison between the proposed strategy and the conventional approach, as illustrated in Fig. 12, reveals several important observations. At higher wind speeds, the system tends to become unstable; however, when the proposed SSRD is implemented at 9 m/s, SSR is fully suppressed. As a result, the active power P_e , electromagnetic torque T_e , and DC-link voltage V_{dc} rapidly return to their nominal values. In contrast, the conventional method fails to adequately control SSR under the same operating conditions, leading to intensified oscillations, as shown in Fig. 12. These results clearly demonstrate that the proposed SSRD achieves faster and more effective oscillation damping than the conventional control method.

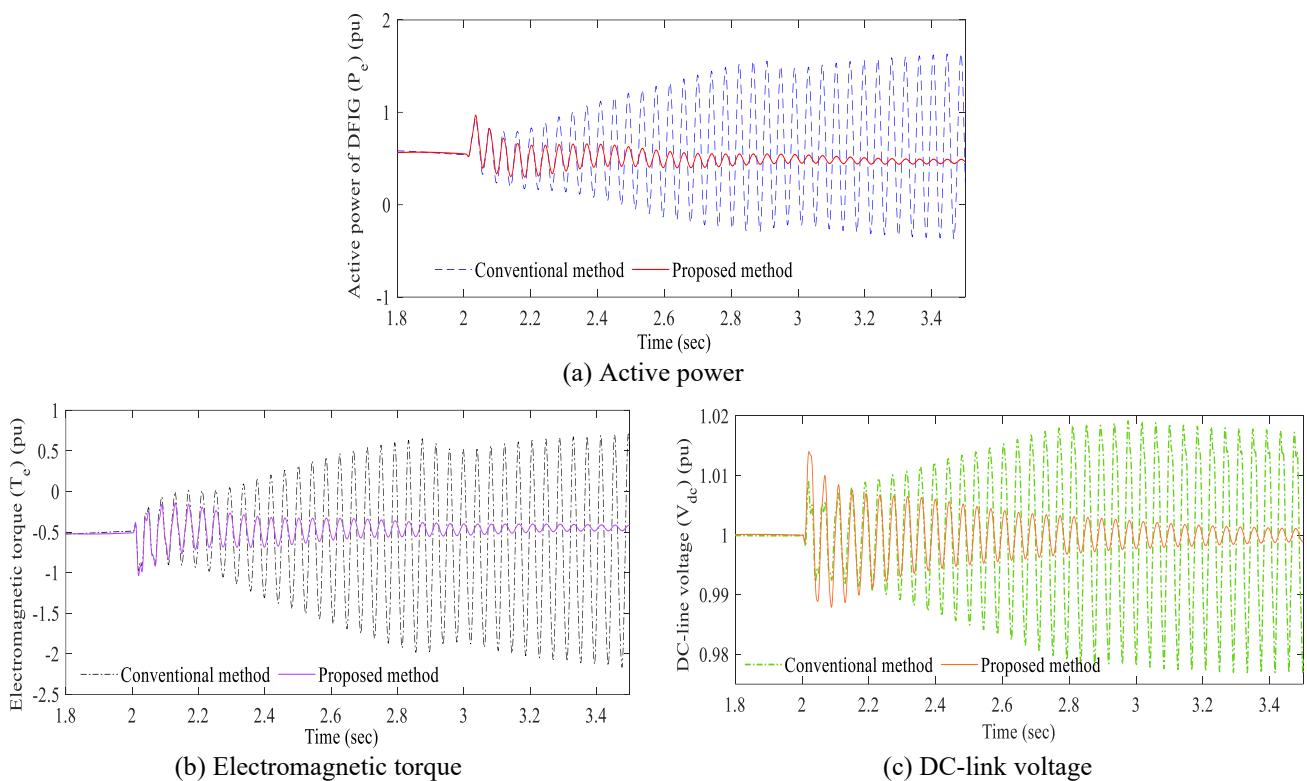


Fig. 12 Dynamic responses of the DFIG-WT system under Case Study 2

Furthermore, Fig. 13 shows a noticeable reduction in harmonic distortion when the proposed technique is applied. The improved damping performance contributes to smoother voltage waveforms and a more stable interaction between the DFIG wind farm and the grid. This behavior highlights the advantage of the proposed method in enhancing power quality under dynamic operating conditions.

From a quantitative perspective, the proposed method achieves a significantly lower maximum active power P_e of 0.9692 pu, compared to 1.841 pu for the conventional approach, while both methods share the same minimum value of -0.7675 pu. This indicates that the proposed strategy effectively limits peak power oscillations, thereby enhancing overall system stability. In terms of electromagnetic torque T_e , the proposed controller produces substantially smaller fluctuations, with a maximum of 0.0189 pu and a minimum of -1.037 pu, whereas the conventional method exhibits much larger swings, ranging from 1.082 pu to -2.816 pu. The reduction in torque oscillations contributes to improved torque stability and reduced mechanical stress on the turbine shaft.

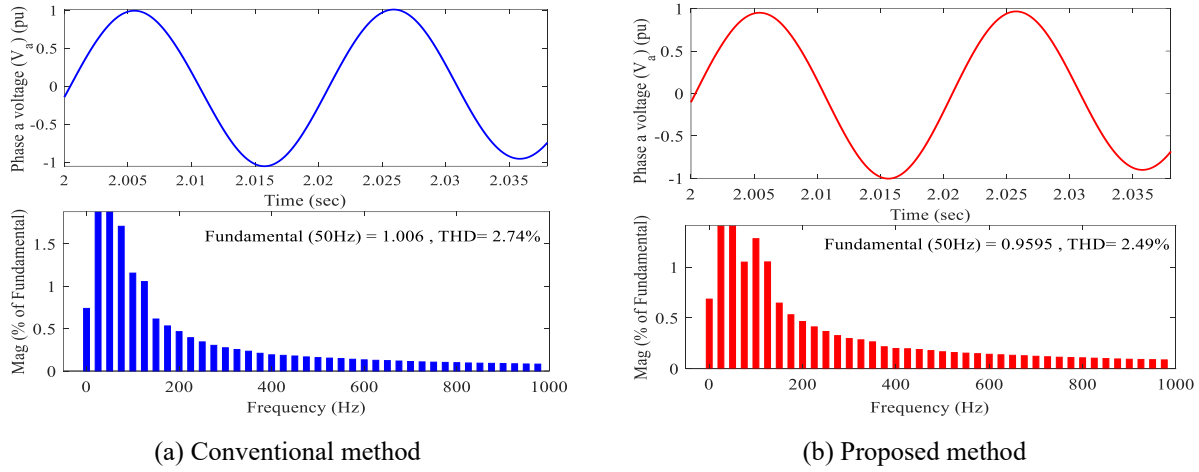


Fig. 13 Phase A voltage waveform and harmonic spectrum at the 575 V bus under Case Study 2

Regarding the DC-link voltage V_{dc} , the proposed approach maintains values closer to the nominal operating range, with peaks of 1.047 pu and troughs of 0.9138 pu. By comparison, the conventional method exhibits wider voltage deviations, reaching a maximum of 1.039 pu and a minimum of 0.9769 pu, indicating inferior voltage stability and a higher susceptibility to voltage fluctuations. Additionally, the THD is reduced to 2.49% with the proposed method, compared to 2.74% for the conventional case, reflecting a clear improvement in power quality through cleaner electrical waveforms, as summarized in Table 5.

Table 5 Statistical comparison of key signals during 2.0 to 3.5 sec under Case Study 2

Parameters	Signal statistics	Proposed method	Conventional method	Parameters	Signal statistics	Proposed method	Conventional method
P_e (pu)	max	9.692e-01	1.841e+00	V_{dc} (pu)	max	1.047e+00	1.039e+00
	min	-7.675e-01	-7.675e-01		min	9.138e-01	9.769e-01
T_e (pu)	max	1.890e-02	1.082e+00	%THD	-	2.49	2.74
	min	-1.037e+00	-2.816e+00	-	-	-	-

4.3. Case Study 3, Wind Speed of 11 m/s and Compensation Level up to 30%

Similarly, the effectiveness of the proposed SSRD was evaluated at a wind speed of 11 m/s with a reduced compensation level of 30% applied at $t = 2$ sec, as illustrated in Fig. 14. The dynamic responses of active power P_e , electromagnetic torque T_e , and DC-link voltage V_{dc} show significantly smaller oscillation amplitudes and faster damping rates when using the proposed method compared to the conventional approach. In contrast, the conventional method exhibits pronounced oscillations in active power between 2 and 2.5 sec, whereas the proposed SSRD rapidly stabilizes the signal to its reference value, demonstrating improved transient stability under low compensation conditions. The numerical values for Case Study 3 are summarized in Table 6.

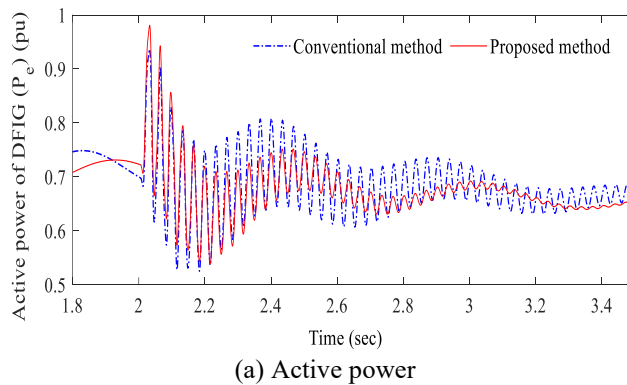


Fig. 14 Dynamic responses of the DFIG-WT system under Case Study 3

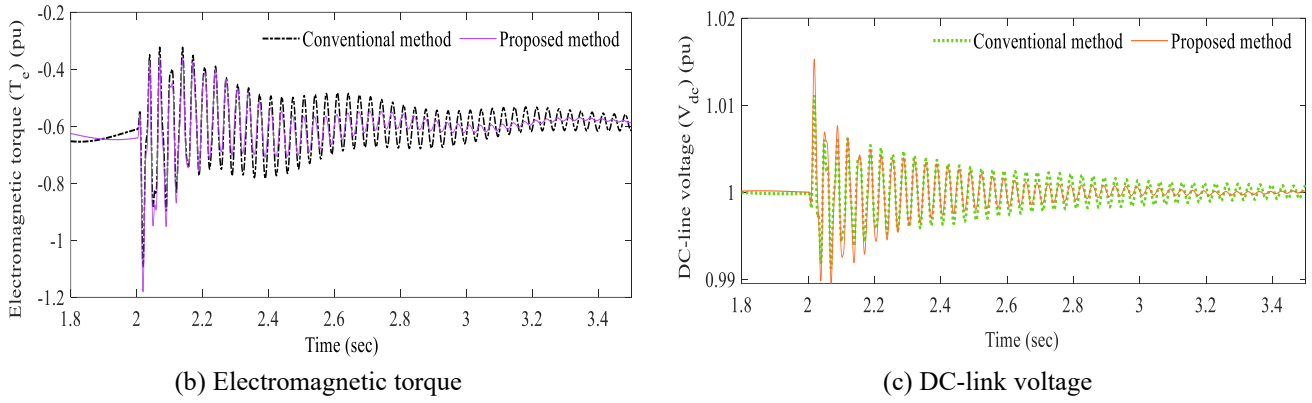


Fig. 14 Dynamic responses of the DFIG-WT system under Case Study 3 (continued)

Furthermore, Fig. 15 shows that the phase A voltage waveform at 575 V bus obtained with the conventional method is more distorted, while the proposed technique maintains a nearly ideal sinusoidal shape. Harmonic spectrum analysis indicates that the fundamental 50 Hz component reaches 0.9991 with the proposed method, surpassing the value of 0.9333 achieved by the conventional approach. Additionally, the THD decreases from 2.366% to 1.996%, confirming enhanced voltage quality and reduced harmonic interference under the proposed control strategy.

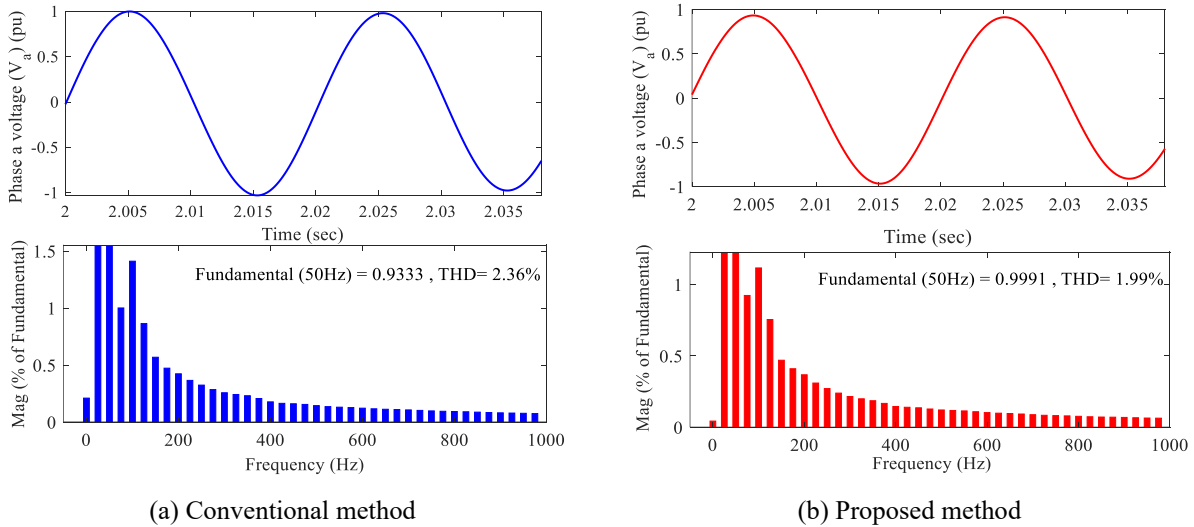


Fig. 15 Phase A voltage waveform and harmonic spectrum at the 575 V bus under Case Study 3

The proposed method exhibits a slightly lower maximum active power P_e of 0.9809 pu compared to 1.023 pu for the conventional method, while both approaches share the same minimum value of -0.7675 pu. This result suggests that the proposed SSRD effectively limits positive power peaks, thereby contributing to improved system stability. For electromagnetic torque T_e , the proposed method shows smaller oscillations, with a maximum of 0.0189 pu and a minimum of -1.181 pu, compared to the conventional method, which reaches 0.02141 pu and -1.094 pu. Although the minimum torque value is slightly lower with the proposed approach, the overall reduction in oscillation amplitude indicates improved torque stability.

Regarding the DC-link voltage V_{dc} , the proposed method maintains values closer to the nominal range, with a maximum of 1.047 pu and a minimum of 0.9168 pu. In contrast, the conventional method exhibits wider deviations, reaching a maximum of 1.039 pu and a minimum of 0.9808 pu, reflecting more severe voltage fluctuations. Additionally, the THD is reduced to 1.99% with the proposed method, compared to 2.36% for the conventional case, indicating improved voltage quality with waveforms closer to a pure sine wave. Overall, in Case Study 3, the proposed SSRD consistently outperforms the traditional method by reducing power and torque oscillations, stabilizing the DC voltage more rapidly, and lowering harmonic distortion, thereby confirming its effectiveness and reliability under low compensation operating conditions.

Table 6 Statistical comparison of key signals during 2.0 to 3.5 sec under Case Study 3

Parameters	Signal statistics	Proposed method	Conventional method	Parameters	Signal statistics	Proposed method	Conventional method
P_e (pu)	max	9.809e-01	1.023e+00	V_{dc} (pu)	max	1.047e+00	1.039e+00
	min	-7.675e-01	-7.675e-01		min	9.168e-01	9.808e-01
T_e (pu)	max	1.890e-02	2.141e-02	%THD	-	1.99	2.36
	min	-1.181e+00	-1.094e+00	-	-	-	-

5. Conclusions

While eigenvalue analysis is a widely used tool for assessing the stability of linear systems, its direct application to finite control set model predictive control (FCS-MPC) controlled doubly-fed induction generator (DFIG) is limited. This limitation arises from the variable switching frequency and the nonlinear nature of the cost function. In this study, system stability and damping performance are therefore rigorously assessed through comprehensive time-domain simulations. The results confirm that the proposed coordinated control strategy maintains a robust stability margin across the entire operating range of the wind farm.

Moreover, the computational efficiency of FCS-MPC supports the feasibility of the proposed coordinated control strategy for real-time applications. Unlike long-horizon model predictive control schemes, the FCS considered in this work evaluates only seven to eight switching vectors per control cycle, which is well within the processing capabilities of modern digital signal processors and field-programmable gate array controllers. This study successfully validates a novel coordinated control strategy for robust SSR mitigation in a series-compensated DFIG-based wind turbine. The proposed approach integrates FCS-MPC in the rotor-side converter with an active SSR damping controller implemented in the GSC. The primary conclusions derived from extensive time-domain simulations under diverse operating conditions are summarized as follows:

- (1) The proposed strategy provides superior dynamic stability by significantly reducing the maximum electromagnetic torque oscillation from values exceeding 1.0 pu under conventional control to approximately 0.02 pu across all validated scenarios.
- (2) The coordinated control consistently reduces the total harmonic distortion of the grid voltage, lowering the distortion level from 2.3% to below 2.0% in critical operating conditions, thereby ensuring cleaner power injection.
- (3) The proposed control scheme ensures rapid stabilization and tight regulation of the DC-link voltage and active power, demonstrating high robustness and reliability under dynamic disturbances and varying operating points.

Conflicts of Interest

The authors declare no conflict of interest.

References

- [1] S. Behera, S. K. Behera, and B. B. Pati, "Impact of DFIG in Wind Energy Conversion System for Grid Disturbances," Proceedings of Engineering and Technology Innovation, vol. 13, pp. 10-19, 2019.
- [2] E. Bounadja, A. Yahdou, W. M. Kacemi, A. Belhadj Djilali, H. Benbouhenni, and A. Iqbal, "A New Third-Order Continuous Sliding Mode Speed and DC-Link Voltage Controllers for a PMSG-Based Wind Turbine with Energy Storage System," Arabian Journal for Science and Engineering, vol. 50, no. 8, pp. 6017-6036, 2025.
- [3] T. A. Zarma, E. Ali, A. A. Galadima, T. Karataev, and S. Usman, "Energy Demand Forecasting for Hybrid Microgrid Systems Using Machine Learning Models," Proceedings of Engineering and Technology Innovation, vol. 29, pp. 68-83, 2025.
- [4] X. Feng, T. Wen, X. Liu, Y. Liu, and Q. Wu, "Mitigating SSR of Series-Compensated DFIG Wind Farms Based on Cascaded High-Gain State and Perturbation Observers," CSEE Journal of Power and Energy Systems, vol. 11, no. 4, pp. 1582-1595, 2025.

- [5] M. M. Islam, K. Sohag, S. Hammoudeh, O. Mariev, and N. Samargandi, "Minerals Import Demands and Clean Energy Transitions: A Disaggregated Analysis," *Energy Economics*, vol. 113, article no. 106205, 2022.
- [6] O. Bialobrzeskiy, A. Postil, and M. Oliynichenko, "Instantaneous Power of a Doubly Fed Induction Generator with the Unbalanced Stator Windings," *Naukovyi Visnyk Natsionalnoho Hirnychoho Universytetu*, no. 4, pp. 98-107, 2025.
- [7] S. Hadavi, M. Z. Mansour, and B. Bahrani, "Optimal Allocation and Sizing of Synchronous Condensers in Weak Grids with Increased Penetration of Wind and Solar Farms," *IEEE Journal on Emerging and Selected Topics in Circuits and Systems*, vol. 11, no. 1, pp. 199-209, 2021.
- [8] X. Xie, X. Zhang, H. Liu, H. Liu, Y. Li, and C. Zhang, "Characteristic Analysis of Subsynchronous Resonance in Practical Wind Farms Connected to Series-Compensated Transmissions," *IEEE Transactions on Energy Conversion*, vol. 32, no. 3, pp. 1117-1126, 2017.
- [9] A. E. Leon and J. A. Solsona, "Sub-Synchronous Interaction Damping Control for DFIG Wind Turbines," *IEEE Transactions on Power Systems*, vol. 30, no. 1, pp. 419-428, 2014.
- [10] B. T. H. Phuong, T. T. Ngoc, P. H. Thanh, and L. Van Dai, "Mitigating Subsynchronous Resonance in Doubly Fed Wind Turbine Induction Generator Using FACTS Devices: A Comparative Case Study," *International Journal of Robotics and Control Systems*, vol. 5, no. 1, pp. 311-332, 2025.
- [11] H. A. Mohammadpour and E. Santi, "SSR Damping Controller Design and Optimal Placement in Rotor-Side and Grid-Side Converters of Series-Compensated DFIG-Based Wind Farm," *IEEE Transactions on Sustainable Energy*, vol. 6, no. 2, pp. 388-399, 2015.
- [12] A. K. Abdulabbas, S. M. Salih, and M. A. Alawan, "The Analysis of Sub-Synchronous Resonance in a Wind Farm for a Doubly-Fed Induction Generator Using Modern Analytical Method," *Iraqi Journal for Electrical and Electronic Engineering*, vol. 20, no. 1, pp. 257-270, 2024.
- [13] J. Yao, X. Wang, J. Li, R. Liu, and H. Zhang, "Sub-Synchronous Resonance Damping Control for Series-Compensated DFIG-Based Wind Farm with Improved Particle Swarm Optimization Algorithm," *IEEE Transactions on Energy Conversion*, vol. 34, no. 2, pp. 849-859, 2018.
- [14] D. Van Hoa, H. H. Bao Nghia, and L. Van Dai, "Optimizing Permanent Magnet Synchronous Motor Control: A Comparative Study of MPCC-Based Techniques," *Eastern-European Journal of Enterprise Technologies*, vol. 135, no. 22, pp. 73-89, 2025.
- [15] F. Meng, D. Sun, K. Zhou, J. Wu, F. Zhao, and L. Sun, "A Sub-Synchronous Oscillation Suppression Strategy for Doubly Fed Wind Power Generation System," *IEEE Access*, vol. 9, pp. 83482-83498, 2021.
- [16] L. Fan and Z. Miao, "Mitigating SSR using DFIG-Based Wind Generation," *IEEE Transactions on Sustainable Energy*, vol. 3, no. 3, pp. 349-358, 2012.
- [17] Y. Wang, Q. Wu, R. Yang, G. Tao, and Z. Liu, "H ∞ Current Damping Control of DFIG Based Wind Farm for Sub-Synchronous Control Interaction Mitigation," *International Journal of Electrical Power & Energy Systems*, vol. 98, pp. 509-519, 2018.
- [18] J. Shair, X. Xie, J. Yang, J. Li, and H. Li, "Adaptive Damping Control of Subsynchronous Oscillation in DFIG-Based Wind Farms Connected to Series-Compensated Network," *IEEE Transactions on Power Delivery*, vol. 37, no. 2, pp. 1036-1049, 2021.
- [19] M. Mokhtari, J. Khazaei, and D. Nazarpour, "Sub-Synchronous Resonance Damping Via Doubly Fed Induction Generator," *International Journal of Electrical Power & Energy Systems*, vol. 53, pp. 876-883, 2013.
- [20] IEEE Subsynchronous Resonance Task Force of the Dynamic System Performance Working Group, "First Benchmark Model for Computer Simulation of Subsynchronous Resonance," *IEEE Transactions on Power Apparatus and Systems*, vol. 96, no. 5, pp. 1565-1572, 1977.
- [21] M. Abdeen, H. Li, S. Kamel, A. Khaled, M. El-Dabah, M. Kharrich, et al., "A Recent Analytical Approach for Analysis of Sub-Synchronous Resonance in Doubly-Fed Induction Generator-Based Wind Farm," *IEEE Access*, vol. 9, pp. 68888-68897, 2021.
- [22] C. N. Dien, H. H. B. Nghia, L. C. Quyen, and L. V. Dai, "Optimizing Permanent Magnet Synchronous Motor Performance Considering Both Maximum Torque Per Ampere and Field Weakening," *International Journal of Intelligent Engineering & Systems*, vol. 18, no. 1, pp. 1121-1136, 2025.
- [23] L. Van Dai, "A Novel Protection Method to Enhance the Grid-Connected Capability of DFIG Based on Wind Turbines," *IETE Journal of Research*, vol. 70, no. 2, pp. 2047-2063, 2024.
- [24] T. V. Thanh, D. T. Viet, N. H. Hieu, and L. Van Dai, "Advanced Frequency Control Strategy for Power Systems with High Renewable Energy Penetration: A Battery Energy Storage System Approach," *An International Journal of Optimization and Control: Theories and Applications*, vol. 15, no. 4, pp. 625-648, 2025.

- [25] A. Younesi, S. Tohidi, and M. R. Feyzi, "An Improved Long-Horizon Model Predictive Control for DFIG in WECS with Variable Sampling-Time," *IET Renewable Power Generation*, vol. 16, no. 3, pp. 517-531, 2022.
- [26] S. Mostafavi, A. Shemshadi, R. Nazari, and H. Yousefkhani, "Utilization of H_∞ Robust and Damping Controllers with Notch Filters to Reduce SSR in Doubly-Fed Induction Generator Wind Farms," *Computers and Electrical Engineering*, vol. 123, part A, article no. 110024, 2025.
- [27] Z. Moradi-Shahrbabak, "Proposed Sub-Synchronous Resonance Damping Controller for Large-Scale Wind Farms," *IET Renewable Power Generation*, vol. 17, no. 13, pp. 3209-3220, 2023.
- [28] M. Abdeen, H. Li, M. A. E. H. Mohamed, S. Kamel, B. Khan, and Z. Chai, "Sub-Synchronous Interaction Damping Controller for a Series-Compensated DFIG-Based Wind Farm," *IET Renewable Power Generation*, vol. 16, no. 5, pp. 933-944, 2022.
- [29] B. Majout, H. El Alami, H. Salime, N. Zine Laabidine, Y. El Mourabit, S. Motahhir, et al., "A Review on Popular Control Applications in Wind Energy Conversion System Based on Permanent Magnet Generator PMSG," *Energies*, vol. 15, no. 17, article no. 6238, 2022.



Copyright© by the authors. Licensee TAETI, Taiwan. This article is an open-access article distributed under the terms and conditions of the Creative Commons Attribution (CC BY-NC) license (<https://creativecommons.org/licenses/by-nc/4.0/>).